ANALYSIS OF SHEAR WAVE GENERATION BY DECOUPLED AND PARTIALLY COUPLED EXPLOSIONS

Jeffry L. Stevens, Heming Xu, and G. Eli Baker

Science Applications International Corporation

Sponsored by Air Force Research Laboratory

Contract No. FA8718-06-C-0007

ABSTRACT

The objective of this project is to investigate the sources of shear wave generation by decoupled and partially coupled explosions, and the differences in shear wave generation between tamped and decoupled explosions, using data analysis and numerical modeling of decoupled and partially coupled explosions.

A perfectly spherical explosion at the center of a perfectly spherical cavity large enough to fully decouple the explosion would generate no shear waves, so all shear waves from decoupled explosions are due to asymmetries in and near the cavity, and to scattering and conversions. We explicitly model the shear waves generated by an explosion offset from the center of a spherical cavity, which causes the shock wave to vary in amplitude and arrival time around the cavity surface. We present a general solution to this problem and calculations of an airshock propagating in the cavity and impacting the cavity wall. The offset explosion has a dipole component and can generate significant shear waves with a modest offset from the center.

We model the Sterling decoupled explosion and show that the near field shear waves observed from that event are likely caused by the cavity shape. The Sterling cavity was approximately spherical except for a flat cavity floor due to melted and recrystallized salt. We model the impact of the shock wave from the explosion on the cavity walls using a 2D Eulerian finite difference code that simulates the evolution of the air shock in the cavity coupled with a 2D Lagrangian finite difference code that simulates the nonlinear region outside the cavity. Calculated shear waves generated by the impact of the shock wave with the cavity floor are in good agreement with the near field observations. The rock adjacent to Salmon was intensely fractured by the explosion, so it is possible that some of these cracks were opened by Sterling. Propagation of the hydrofractures driven by the Sterling explosion is modeled by coupling stress wave dynamics in rock with fluid mechanics in the fractures. The results show that the cavity pressure is insufficient to overcome the overburden to propagate fractures into rock, except for the area immediately below the explosion on the cavity floor. The simulations match the first arrivals of both P and S waves quite well, however the observations also have substantial P and S coda, which are not reproduced by the calculations.

Records at a common set of local stations of a tamped and subsequent water filled cavity explosions provide an opportunity to distinguish between shear wave generation mechanisms. The P and S spectra of the tamped and decoupled explosions are similar, except for a 9 Hz bubble pulse in the P, but not the S spectra of the decoupled explosions. This is inconsistent with shear wave generation by P-wave scattering. The high frequencies and 600 m depth are inconsistent with generation by Rg scattering. Synthetic modeling demonstrates that a spherical explosion source is insufficient to generate the observed shear waves, but they are predicted by compensated linear vector dipole (CLVD) synthetics. Finally, the observed P and S travel times from 1 to 5 km are consistent with CLVD synthetics, that is, with generation at the source. While not inconsistent with scattering to S, such scattering would have to be nearly instantaneous, occur very close to the source, and not occur at greater distance from the source, as the S arrivals are impulsive, temporally compact, and move out smoothly with distance.

OBJECTIVES

The objective of this project is to investigate the sources of shear wave generation by decoupled and partially coupled explosions, and the differences in shear wave generation between tamped and decoupled explosions. This is being accomplished through a program of data analysis and numerical modeling of decoupled and partially coupled explosions.

RESEARCH ACCOMPLISHED

Introduction

This project investigates shear waves from decoupled and partially coupled explosions, focusing on source mechanisms for shear waves, constrained by observations and numerical simulations. Although a nuclear explosion detonated at the center of a perfect spherical cavity large enough to decouple the explosion would generate no shear waves (other than conversions due to the earth's surface and scattering), in fact no cavity has perfect spherical symmetry, nor is the explosion exactly at the center, and shear waves have been observed from all decoupled explosions, even quite close to the source.

In this paper, we examine the following:

1. We present a general solution to the problem of shear waves generated by an explosion offset from the center of a spherical cavity, which causes the shock wave to vary in amplitude and arrival time around the cavity surface, followed by calculations of an airshock propagating in the cavity and impacting the cavity wall.
2. We present a detailed numerical model of the Sterling experiment.
3. We perform data analysis and numerical modeling of shear waves from Russian nuclear explosions in water-filled cavities.

Shear Waves from a Non-Isotropic Explosion Source

We model the seismic waves from a non-isotropic explosion source, specifically an explosion offset from the center of a spherical cavity, using a modification of the method developed by Stevens (1980) to solve the problem of seismic waves generated by an explosion in a prestressed elastic medium. The general solution for the seismic wave field from a set of tractions applied to the inside of a spherical cavity is given by

$$u = -\int_{\Sigma} u \cdot T(G) \cdot \hat{n} dA + \int_{\Sigma} G \cdot T(u) \cdot \hat{n} dA, \tag{1}$$

where Σ is the cavity surface, *u* on the left side of the equation is the displacement at any location outside the cavity, and *u* inside the integral is the displacement on the cavity wall. *G* is the elastic Green's tensor in spherical coordinates, and *T* is the stress operator. The second term represents the response of the medium to the applied stress from the explosion, and the first term represents the additional motion due to the response of the cavity wall Equation 1 can be solved by expanding the displacement, traction and Green's tensor in vector spherical harmonics. The case of interest here is shown in Figure 1 (left), where the explosion source is initially offset from the center of an air-filled cavity of radius R by a distance d. The right side of Figure 1 shows the calculated P and S waves from the explosion. The offset from the center causes the shock wave to impact the side of the cavity closest to the explosion earlier and with greater force than the opposite side of a cavity. This is equivalent to a dipole source acting in the direction of the offset, and as illustrated, can generate S waves comparable in amplitude to the initial P wave. Note that the offset in origin breaks the symmetry of the problem except for axisymmetry about the offset axis. If the offset is oriented horizontally relative to the surface, strong SH waves will be generated. Zhou and Harkrider (1992) similarly found that a point explosion offset from the center in a solid-filled spherical region embedded in a whole space acts primarily as a dipole source.

Figure 2 shows the results of a full nonlinear calculation of a 0.38 kt explosion offset by 5 meters from the center of a 9 meter radius air-filled cavity in strong granite. Overburden pressure is 130 bars. The explosion is almost fully decoupled, but there is some nonlinear deformation within a few meters of the cavity. The results show strongly asymmetric P waves as a function of angle around the cavity, and substantial S wave generation on the transverse component.

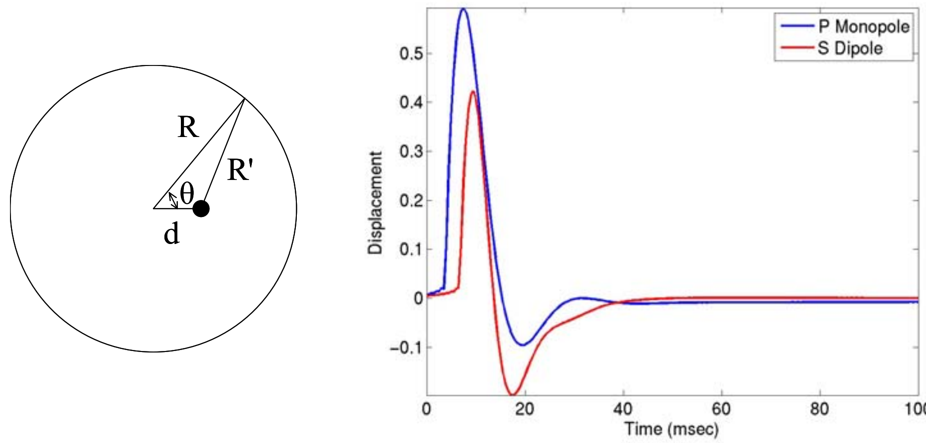

Figure 1. Calculated P and S waves (right) for an explosion in an air-filled cavity with the origin of the explosion offset from the center (left). In this example the cavity radius is 17 m and the offset from the center is 8.5 m.

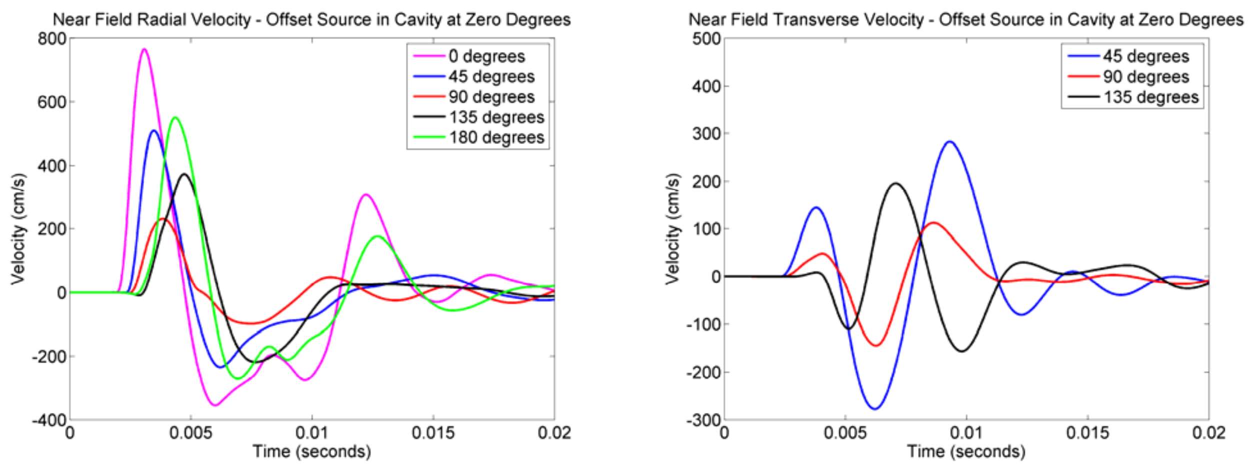

Figure 2. Nonlinear calculation of near field radial and transverse velocity at a distance of 20 meters from an explosion in a 9 meter radius cavity in granite, offset from the center by 5 meters. The left figure shows radial velocity, which is mostly P wave, and the right shows transverse velocity, which is mostly S wave, at angles of 0, 45, 90, 135, and 180 degrees as illustrated in Figure 1. Transverse motion is zero by symmetry at 0 and 180 degrees, but is strong at 45, 90, and 135 degrees. Waveforms are low-pass filtered at 200 Hz.

Sterling Axisymmetric Calculations

The 0.38 kt nuclear Sterling experiment was detonated at the center of the cavity excavated by the 5.3 kt Salmon test. The post-Salmon cavity was found to be approximately spherical with a 17-m radius, except that a pool of molten salt recrystalized in the bottom of the cavity with the pool floor approximately 10 m from the center (Langston, 1983). In this configuration, the explosive pressure waves reached the floor pool and spherical wall at different times and strength, resulting in asymmetric effects including SV wave generation. Langston (1983) constructed kinematic source models to simulate the observations, and his results suggested that the SV waves were radiated primarily by induced normal faulting occurring beneath the cavity. In this study, we simulate the Sterling explosion using the actual cavity geometry and salt properties obtained from the Salmon explosion modeling.

Methodology

We model the Sterling event using the two-dimensional axisymmetric Lagrangian finite difference code CRAM, coupled with the Eulerian code STELLAR. The grid setup is similar to that for the Salmon event calculation

(Stevens et al., 2006). To successfully simulate waves due to the cavity explosion, the initial grid must be in equilibrium so that the motions due to the empty cavity under overburden pressure are close to zero. The equilibrium solution is obtained by running CRAM in an overdamped mode with an initial approximate solution until motions become negligible throughout the CRAM computational grid. The early time interactions between the air shock due to an explosion and the surrounding salt interaction are simulated with STELLAR and then the results at 2.627 ms are overlaid onto the CRAM grid for calculating wave propagation at later times.

Comparisons between observations and simulations

Figure 3 shows the STELLAR results at 2.6 msec. The velocity, pressure and plastic work distribution are consistent with the non-spherical cavity geometry. The highest plastic work is found below the salt floor and indicates salt hardening. Figure 4 shows the horizontal-radial and vertical velocity data along with the numerical calculations. The observed P wave amplitudes and pulse widths are predicted quite well using the Rimer/Cherry salt model (Rimer and Cherry, 1982) at all 8 near cavity stations although our calculations show less complex P wave coda prior to SV arrivals than observed. SV are well predicted at the shot level stations (middle 3 figures) and below (bottom 2 figures). Most striking is the comparison at the two deeper stations (bottom 2 figures) where the predicted polarity and amplitudes of the SV waves are in excellent agreement with the observations. The calculated SV coda is also less complex than observed. The calculated SV waves at the stations above the shot level are smaller than observed, which could be due to some additional asymmetry in the shock arrival time on the upper cavity wall not modeled in the calculations. The good agreement between data and simulations implies that, not only does the shape of the cavity explain the observations, but that the empirical salt model used in the calculation is adequate to describe the salt's properties even at lower stress.

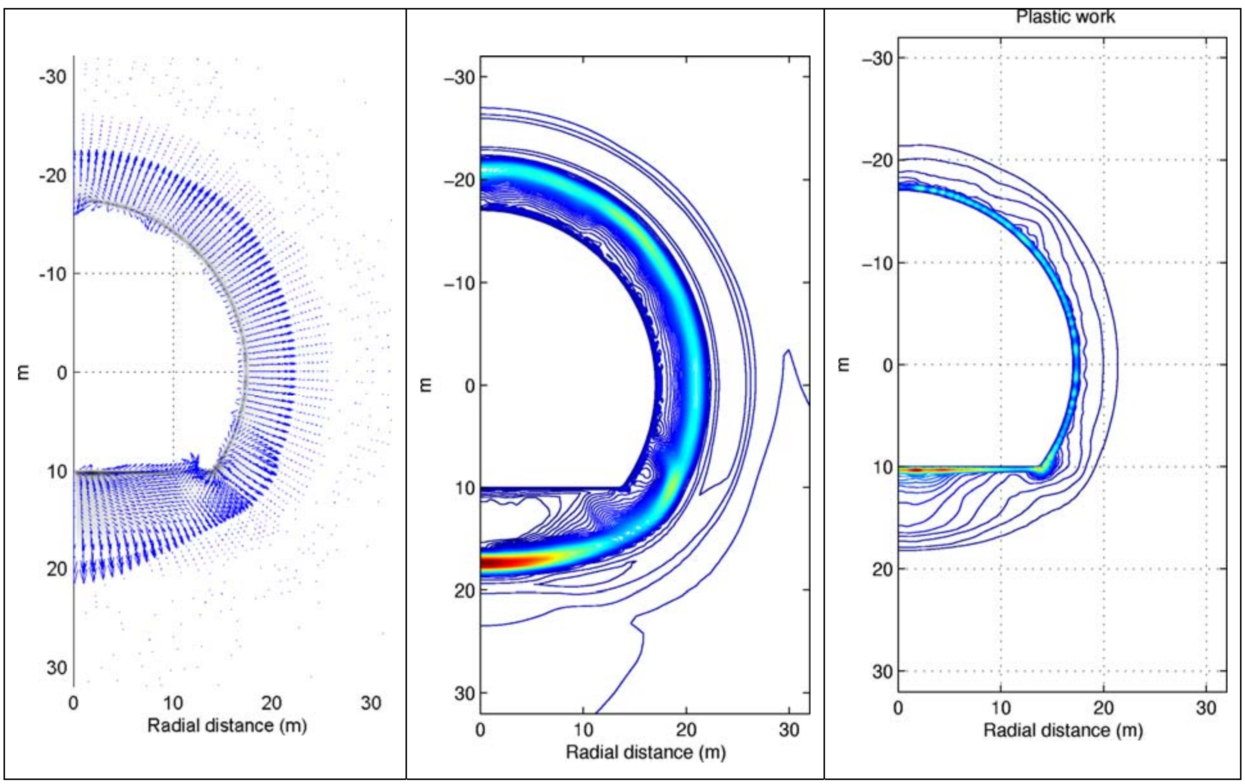

Figure 3. Interaction between the air shock and the salt calculated from STELLAR at a time of 2.627 msec. Left: particle velocity vectors. Middle: pressure contours. The maximum pressure is 2.8 kbar at 7m below the salt floor. Right: plastic work distribution. The maximum plastic work incurred is about 5×10^6 ergs/cm^3 at the pool floor, corresponding to the yield surface of 680 bars. The higher plastic work indicates the higher yield surface (material hardening).

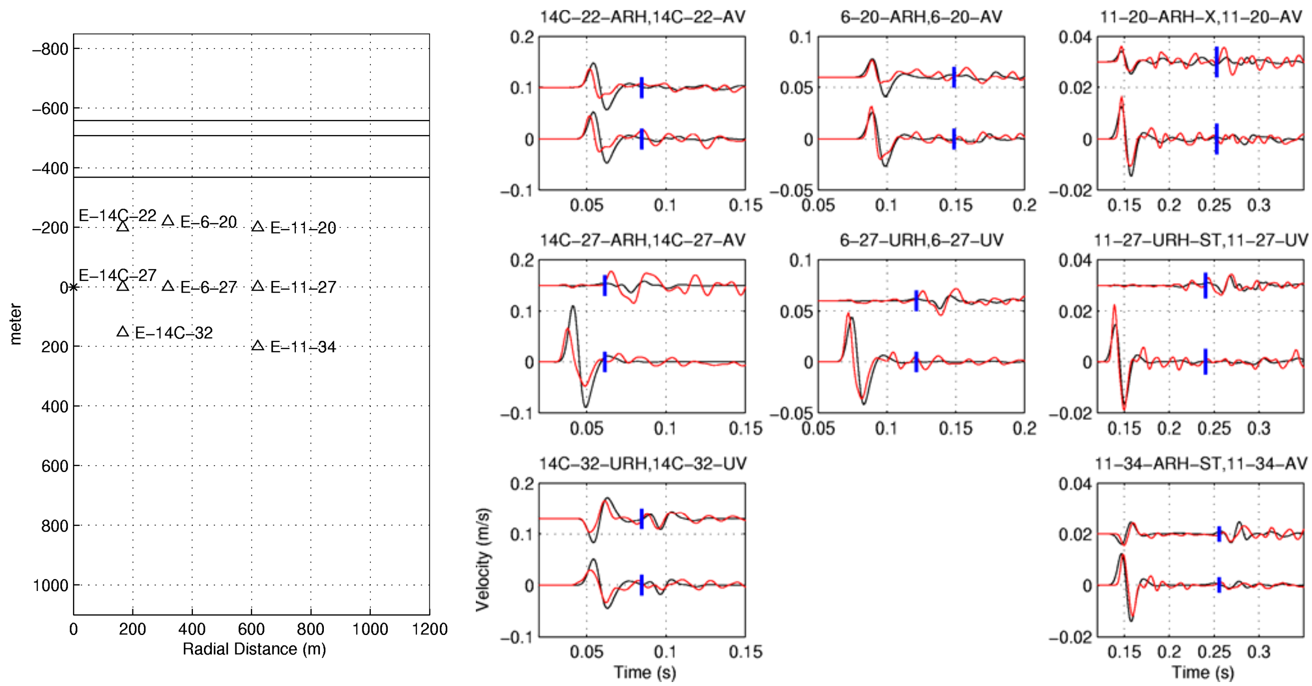

Figure 4. Left: stations for comparison of Sterling data and calculations. Right: Observed (red lines) and synthetic (black) waveforms at near-cavity locations in salt. The top curve in each plot represents the vertical component (positive up) and the bottom curve represents the horizontal radial component. The bold vertical bars denote the theoretical SV arrival time (vs=2540 m/s). The agreement on P wave arrivals and amplitudes is striking, and the agreement on S wave arrivals and amplitudes is better for the shot-level locations and below than for above shot-level stations.

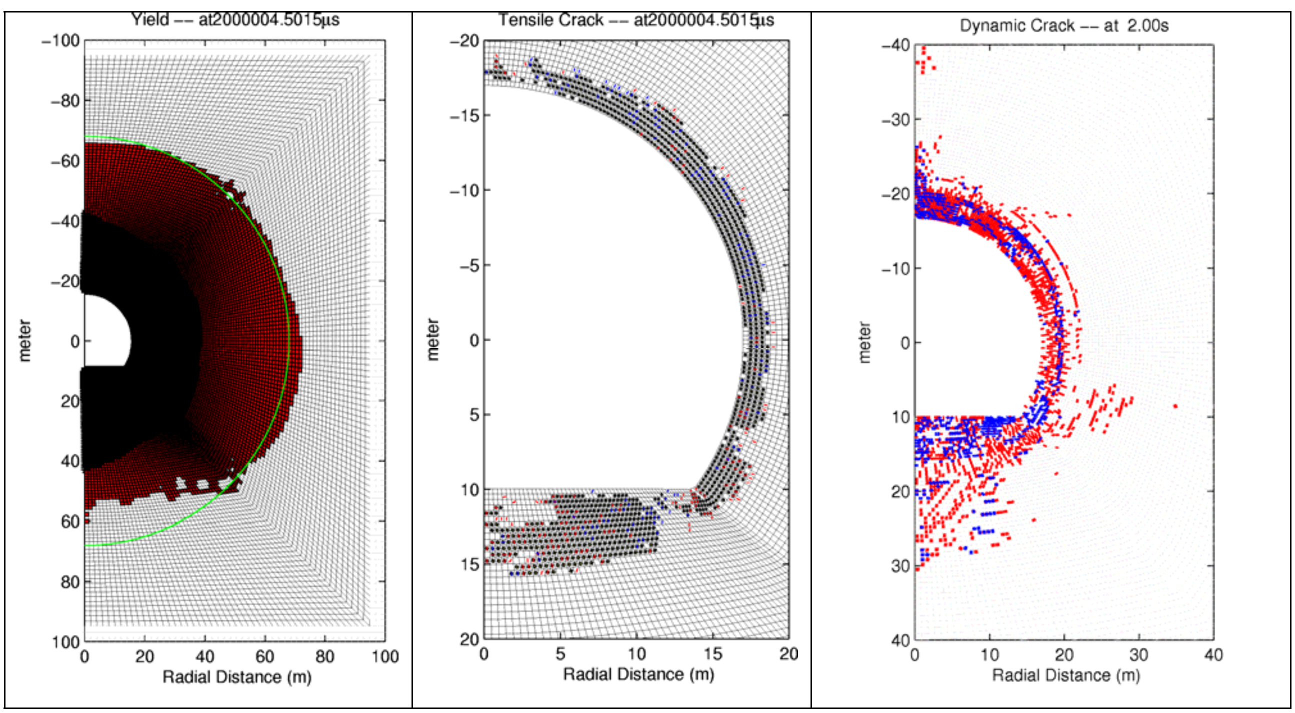

Figure 5. Left: nonlinear deformation distribution due to the Sterling explosion. The green circle is drawn to highlight, by contrast, the nonsphericity of the yield region. Middle: tensile crack distribution due to the Sterling explosion. Tensile cracks open only near the cavity wall. No spall is observed in the calculation. Right: locations where dynamic fractures could occur.

Nonlinear deformation and cracking

Figure 5 shows the nonlinear deformation and tensile cracks from the Sterling calculation. This is an overburied cavity explosion and so the high overburden pressure limits the yield region to about 65 m above and to the right of the cavity, and to less than 60 m below. The Rimer/Cherry salt model hardens after accumulating plastic work, and so the region below the cavity, which experienced the highest shock pressure, also hardened the most, limiting the extent of the nonlinear zone below the cavity. This causes additional asymmetry in the outgoing waves, adding to SV generation.

We also performed two sets of tests to see where hydrofractures could occur (see Nilson et al., 1991; Stevens et al., 2006). The right panel of Figure 5 shows the fracture locations if the entire surrounding salt is pressurized by the cavity. This calculation depicts the preferred pathway for the possible fractures driven open by the cavity pressure. It shows that the vertical fracture near the axis of symmetry below the cavity floor is more likely to propagate due to higher shock impact than at other locations but its extension is limited to 20 meters into the salt. To test Langston's conjecture on the kinematic fault geometry, we also modeled a single preexisting conical crack connecting to the outer bottom edge of the cavity. The results indicate that the crack at that location could not be driven open in tension by the cavity pressure because the overburden pressure is too high to allow it to open, as implied by the right panel of Figure 5.

Incidence dependence of initial S and S-coda waveforms indicates multiple S-wave sources

We observe variations in SV polarity with incidence, not just for the initial arrival, but also in the later S coda. Besides polarity, timing and similarity of waveforms throughout the coda can provide insight into the mechanism that generates it. If coda S-waves are generated at or very near the cavity, they will have the same delay as direct S at all stations along similar ray paths from the cavity. If the coda is generated by scattering at some distance from the cavity, or even by nonlinear deformation at 40 to 50 m from the cavity, the arrivals will move out with distance at a different rate than direct S and so the coda waveforms will not be similar along a given radius out from the cavity. We use recordings at three distances, at, above, and below the shot point to assess the dependence of different parts of the S-wave record on incidence and to assess whether the coda is similar.

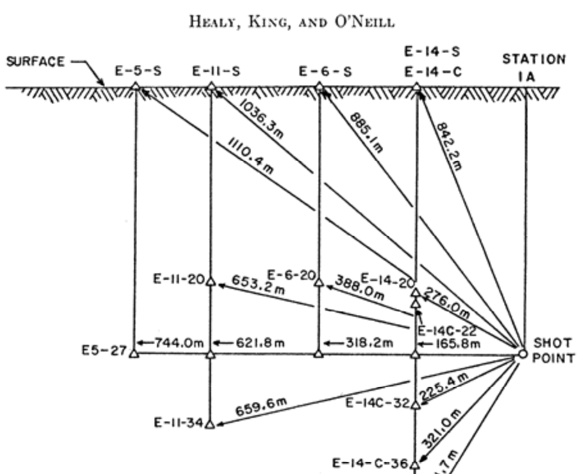

Figure 6. (from Healy, et al., 1971). Locations of near field strong motion instruments.

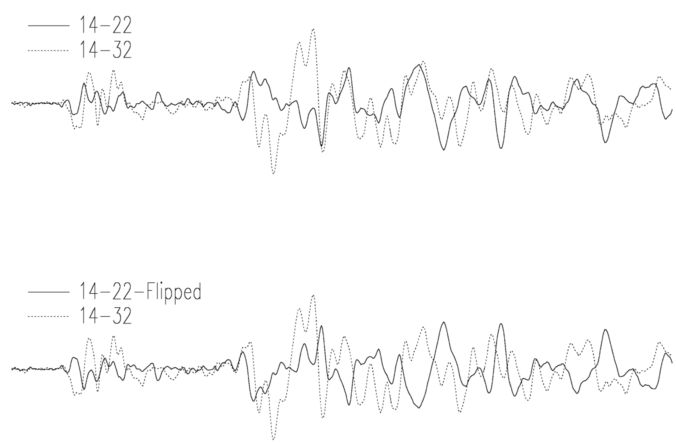

Figure 7. VT component records from 14–22 (solid, above shot level) and 14–32 (dotted, same distance below shot level) aligned on the predicted S time of 0.581 seconds. The top set of traces are normal polarity. The polarity of the above-shot-level record is flipped in the bottom pair of traces.

Figure 6 shows the locations of the instruments. To illustrate the nature of the Sterling S-waves, we first compare records at the same distance, 225 m from the source, so all similar phases should be aligned, but from stations 153 m above and below shot level respectively (Figure 7). The records are rotated in the SV plane normal to the radial, to minimize P and maximize SV. We refer to that as the vertical-tangential (VT) component, to distinguish it from the component normal to the radial, but in the horizontal plane. The above-shot-level trace is plotted solid, and the below-shot-level trace is dotted. The traces are overlain, both with normal polarity (above) and with reversed polarity (below) for the above shot record. The large S-coda traces overlay very well beginning ~0.02 seconds after the predicted S-wave time of 0.58 seconds. The lower two traces, with the above shot record flipped, show that the initial S-waves (0.58 to 0.585 seconds) have opposite polarity above and below shot level. This suggests two mechanisms may be operating. The first has a radiation pattern with incidence. No radiation pattern in the coda can be discerned from these data.

Figure 8 shows multiple above, at, and below shot records aligned on the predicted S-wave time, given a velocity of 2.53 km/s, filtered from 30–200 Hz to eliminate differences due to attenuation at the more distant stations, and overlain. Records at the same or similar incidence have similar waveforms from the initial S throughout the coda, indicating that the bulk of the energy is coming directly from the source.

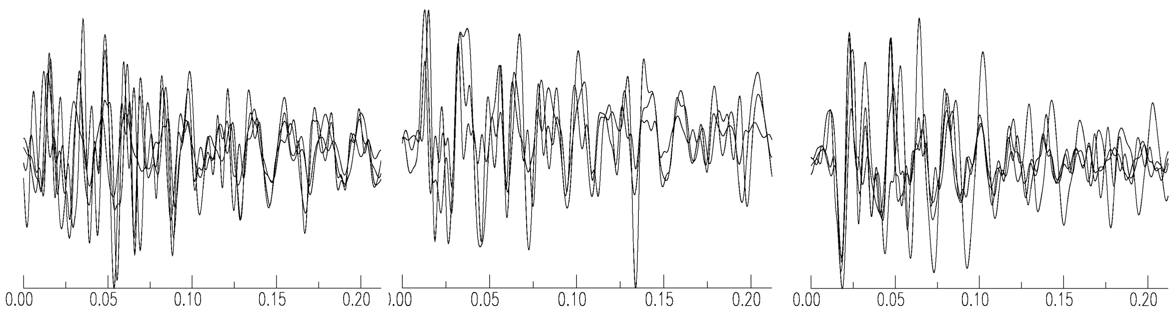

Figure 8. Overlain above (left), at (middle), and below (right) shot point VT component records aligned by the predicted S-wave time at 2.53 km/s, and filtered from 30 to 200 Hz. Above shot point records are from stations 11-20, 14-20, 14-22, and 6-20; at shot point records are from 166, 318, and 622 m distance; and below shot point records are from stations 14-32, 14-36, 14-39, and 11-34.

We next stack each of these sets of records. Figure 9 illustrates the differences between the stacks of waveforms recorded at different take-off angles. The stacks at and above shot level have the same first arrival polarity, opposite that of the below shot level records. The at and below shot level records, however, become similar after 50 ms, indicating a change in radiation pattern with time. Finally we note the strong periodicity of the coda, at approximately 60 Hz, which could suggest oscillations of the cavity itself or the volume of nonlinear deformation immediately around the cavity. There are some differences between observations in Figures 7 and 9, due to frequency content. Further analysis may allow us to distinguish frequency dependence of the source location and radiation with time.

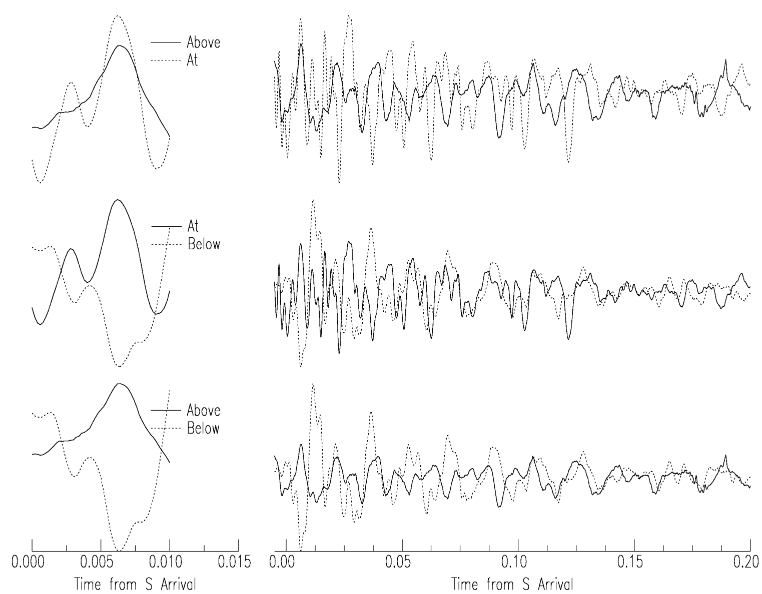

Figure 9. Overlain stacks of above and at (top), at and below (middle), and above and below (bottom) shot point records shown in Figure 8. The initial 0.01 seconds of S are shown to the left, and the waveforms from initial S through the coda are shown on the right.

To recap the observations and implications of Sterling S-waves, stacks of coda from at, above, and below shot level records show that the coda are similar at similar incidence. This implies that the S-wave coda source is located at or very near the cavity, and has a radiation pattern with incidence. The radiation pattern differs from that of the initial S-wave, suggesting a different mechanism from that of the initial S.

Explosions in Water-Filled Cavities

We are examining records from a unique series of explosion, a tamped 27 Kt explosion at 597 m depth in salt at Azgir, followed by four very small explosions (yields 0.35, 0.10, 0.01 and 0.08 kt) in the water-filled, 32.5 m radius, cavity of the original explosion. These are effectively decoupled, in that the small explosions do not cause significant nonlinear deformation of the cavity, but provide large signals as the pressure is much greater in water than it would be in an air-filled cavity. Local radial and vertical component records are available at common stations for multiple events, and 3-component records are generally available from stations at 20 km or more distance, and from several closer stations. All of the explosions generated shear waves. We present time and frequency domain observations that bear on their source, specifically, alignment of the S minus P-wave times, and the presence or absence of a bubble-pulse peak in S- and P-wave spectra.

Figure 10 shows the overlain Hilbert transformed radial and the vertical records at 7.8 km from the 0.01 Kt explosion (bottom), and corresponding explosion (top) and CLVD synthetics (middle), which help us to identify the shear waves. Records are filtered from 5 to 15 Hz, as the data are noisy below 5 Hz. Times are relative to initial P, as absolute times are unknown. Synthetic seismograms use the structure described in Murphy et al. (2001), overlain on a more general Azgir structure (Table 1). The initial P is somewhat complex in both data and synthetics. The secondary arrival 0.4 seconds after P could admit a number of explanations, including P-to-S conversion from the sediment-rock interface beneath the station. Finding a unique explanation is unlikely, but the arrival is too early to be anything but scattered P and so can be used to represent the P source spectrum. The latter part of the next arrival, at ~1.4 seconds after P in the data, is retrograde elliptical, and there are similar arrivals in both sets of synthetics. We typically observe near source explosion shear waves to have retrograde elliptical particle motion consistent with their identification as higher mode Rg. The large S arrival at 3.5 seconds after P in the CLVD synthetics is consistent with an S group velocity of 1.5 km/s, with a P-wave velocity of 4 km/s, so the large S arrival appears to have been trapped in the low velocity surface layer. The amplitude in the data increases before that synthetic arrival, although it only becomes retrograde elliptical again at the approximate time of the synthetic arrival. That's consistent with the earlier part of that large arrival being multiple higher Rg modes (which make up S), with a single isolated higher mode at the end. Identification as S is also consistent with large S arrivals at 1.5 km/s in other records. To compare spectra of these records, we use initial P to 1.1 seconds after to isolate just P, and from 1.9 to 3.1 seconds after P to isolate S.

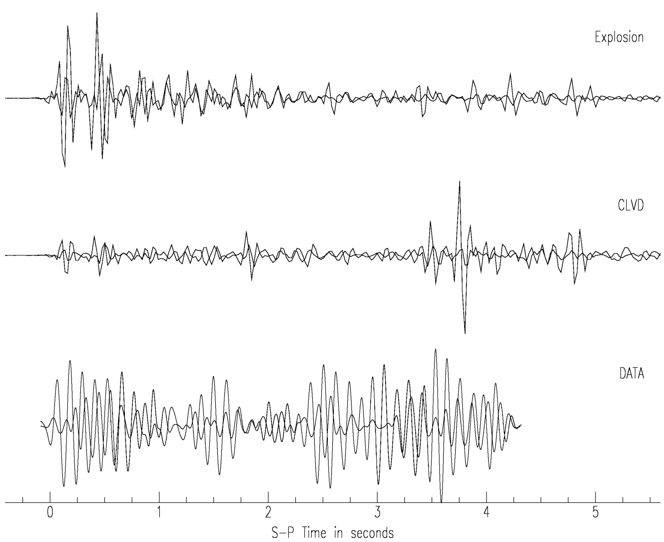

Figure 10. Overlain Hilbert transformed radial and vertical component spherical explosion (top) and CLVD (middle) synthetics at 7.8 km, for 597 m depth, and corresponding records from AZ24, the 0.01 Kt explosion (bottom).

Table 1. Azgir velocity model. Second layer represents anhydrite cap on massive salt dome.

Thickness (m)	Vp	Vs	Density	Qp	Qs
0.240	1.50	0.60	2.00	40	25
0.056	2.20	0.95	2.00	60	35
5.0	4.25	2.40	2.2	200	150
2.0	5.2	2.95	2.30	600	500
2.0	5.889	3.306	2.549	300	0
19.97	5.935	3.332	2.566	333	0
10.00	6.284	3.527	2.693	352	0
12.00	8.357	4.691	3.449	394	0
115.00	7.980	4.479	3.312	403	0

Bubble pulse signature in P- but not S-wave spectra

Murphy et al. (2001) showed that peaks in the decoupled explosions' spectra could be explained by bubble pulse resonances near 8 to 10 Hz, where the extent of the pulse is damped differently depending on the amplitude of the reflected shock wave. A bubble pulse resonance peak is clear in each of the decoupled explosions' P spectra (red) at 7.8 km, but is absent from the tamped explosion's P-spectra (Figure 11). If the shear waves are dominated by pS (as predicted for a low velocity structure), they should be similar to the P-wave spectra and should have the same resonance peak. The peak is absent, however, from the S spectra, indicating that the S is not simply scattered from P.

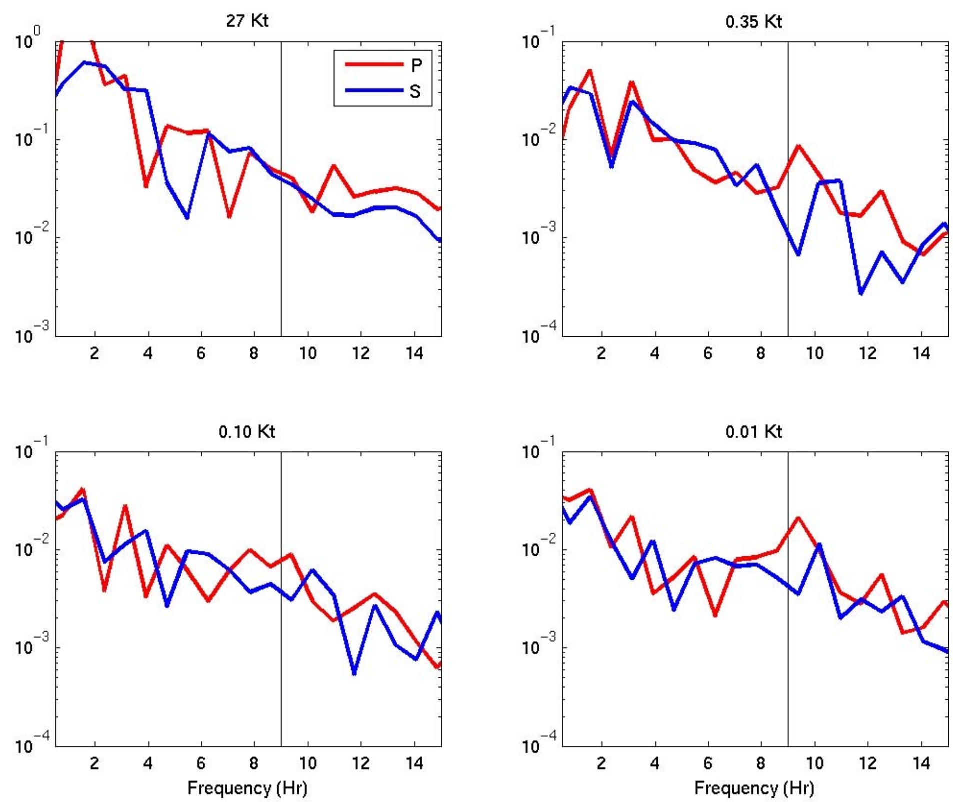

Figure 11: P and S spectra of the tamped and the three decoupled explosions recorded at 7.8 km

If the S-wave comes directly from the source, then the data S-P times plotted vs distance should be similar. Event AZ25, the 0.08 Kt explosion, was recorded at 6 stations, at 0.82 to 4.6 km from the source. Figure 12 shows the data and CLVD synthetic record sections and the P and S picks. The data S-P times are very similar to those of the CLVD synthetics (the explosion synthetics do not reproduce the S-phase). A fit to just the measured S-P times from data intersects zero distance at 0.36 seconds. The same fit for synthetics intersects at 0.30 seconds. Consistent S-P times for data and synthetics suggests that the shear waves must either be generated at the source or scattered from very near the source.

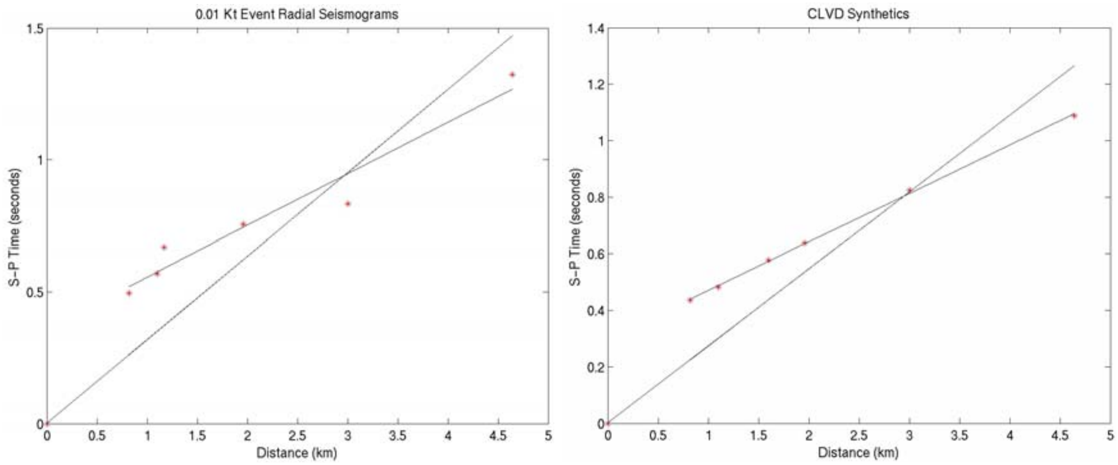

Figure 12. S-P arrival times from event AZ25 (left) and CLVD synthetics (right). Lines are fits to S-P times vs. distance.

CONCLUSIONS AND RECOMMENDATIONS

We find that source asymmetry including, for example, an explosion offset from the source of a spherical cavity can lead to significant asymmetry in seismic waves and generation of S waves. We performed a detailed numerical model of the Sterling decoupled explosion and find that the near field waveforms including near field shear waves can be explained by the cavity shape and the asymmetry caused by varying impact of the explosion shock across different parts of the cavity. However, the S coda continues much longer and at higher amplitude than predicted by the simulations. Analysis of observations from explosions in water-filled cavities shows that S waves are always present, and that they are generated at or very close to the source.

REFERENCES

Healy, J., C. King, and M. O'Neill (1971). Source parameters of the Salmon and Sterling nuclear explosions from seismic measurements, *J. Geophys. Res*. 76: 3344–3355

Langston, C.A. (1983). Kinematic analysis of strong motion P and SV waves from the Sterling event. *J. Geophys. Res.* 88: 3486–3497

Murphy, J. R., D. D. Sultanov, N. Rimer, and B. W. Barker (2001). Seismic source characteristics of nuclear explosions in water-filled cavities, *Pure Appl. Geophys.* 158: 2,105–2,121.

Nilson, R., N. Rimer, and E. Halda (1991). Dynamic modeling of explosively driven hydrofractures, *J. Geophys. Res.*, 96: B11, 18,081–18,100.

Rimer, N. and J. T. Cherry (1982). Ground motion predictions for the Grand Saline experiments, S-CUBED VSC-TR-82-25.

Stevens, J. L. (1980). Seismic radiation from the sudden creation of a spherical cavity in an arbitrarily prestressed elastic medium, *Geophys. J. R. Astr. Soc.* 61: 303–328.

Stevens, Jeffry L., Heming Xu, and G. Eli Baker (2006), Analysis of shear wave generation by decoupled and partially coupled explosions, in *Proceedings of the 28th Annual Seismic Research Review: Ground-Based Nuclear Explosion Monitoring Technologies*, Vol. 1, pp. 693–703.

Zhou, L. and D. G. Harkrider (1992). Wave fields from an off-center explosion in an embedded solid sphere, *Bull. Seism. Soc. Am*. 82: 1,927–1,955.